DOI: 10.13009/EUCASS2019-522

Numerical Simulation of Instabilities Evolution in a High-Speed Boundary Layer with Crossflow Jet Injection

Andrey V. Novikov[⋆,⋆⋆] *and Alexander V. Fedorov*[⋆⋆,⋆]
[⋆]*Central Aerohydrodynamic Institute (TsAGI)*
1 Zhukovsky Street, Zhukovsky, Russia, 140180
[⋆⋆]*Moscow Institute of Physics and Technology (National Research University)*
9 Institutskiy per., Dolgoprudny, Russia, 141701
AndrewNovikov@yandex.ru · fedorov@falt.ru

Abstract

Numerical simulations of three-dimensional disturbances generated near a wall underexpanded jet in a Mach 5.4 flat-plate boundary layer are carried out. The Navier–Stokes equations for compressible perfect gas are integrated using the in-house solver implementing an implicit finite-volume shock-capturing scheme with the second-order approximation in space and time. The wall normal injection through a circular hole forms an underexpanded jet of barrel shape resembling an isolated roughness element. The jet induces a system of vortices propagating downstream. The vortices are destabilized at a short distance leading to rapid nonlinear breakdown and formation of a "young" turbulent wedge. The vortex structure, its instability and breakdown to turbulence resemble those induced by an isolated roughness element. The disturbances evolution is analyzed through Q-criterion visualizations, wall pressure spectra, and skin friction coefficients. Results show that the normal wall injection effectively trips the boundary layer.

1. Introduction

In some applications of high-speed aerodynamics, the turbulent boundary layer is more preferable than the laminar one. For example, due to the small size of the Hyper-X flight test vehicle, natural laminar-turbulent transition (LTT) was not expected to occur prior to the inlet. A laminar boundary layer ingested into the engine would be more susceptible to flow separations and thus reduced performance [1], so artificial passive or active trip devices are required. Such devices were intensively investigated experimentally [2, 3] but physical mechanisms associated with the forced transition are still not fully understood. This gap can be bridged with the help of numerical simulations providing details of the tripping process which are not accessible in experiments. Passive LTT forcing via isolated or distributed roughness elements are being studied now days using direct numerical simulations [4, 5]. Active devices, like wall injection, have received less attention and the publications on the subject are sporadic, whereas these devices have obvious advantages over passive trips. We are aware of only one paper [6] related to numerical simulations of LTT induced by the wall injection.

The present paper provides a feasibility study of high-speed boundary layer tripping by wall blowing of microjet in crossflow. Numerically investigated is the evolution of three-dimensional (3-D) disturbances formed near an isolated underexpanded jet injected into a flat plate boundary layer at free-stream Mach number 5.4. Since these simulations do not use artificial sources of unsteady disturbances, instabilities are excited by the numerical noise that mimics natural conditions in low-disturbance environment typical for free flights. The in-house code HSFlow [7] is used to solve Navier – Stokes equations for viscous compressible flows of perfect gas. Main features of the disturbance evolution are explored using 3-D visualization of the flow fields, spatial-temporal spectra of disturbances and the skin friction distributions.

2. Problem formulation and numerical method

2.1 Governing equations and numerical method

The equations to be solved are the Navier–Stokes equations for 3-D unsteady compressible flows. The fluid is assumed to be a perfect gas (air) with the specific heat ratio $\gamma = const$ and Prandtl number $\mathrm{Pr} = const$. The equations are employed in conservative dimensionless form

$$\frac{\partial \mathbf{Q}}{\partial t} + \frac{\partial \mathbf{E}}{\partial \xi} + \frac{\partial \mathbf{G}}{\partial \eta} + \frac{\partial \mathbf{F}}{\partial \zeta} = 0,$$

where (ξ, η, ζ) is a curvilinear coordinate system for the computational grid, $x = x(\xi, \eta, \zeta)$, $y = y(\xi, \eta, \zeta)$, $z = z(\xi, \eta, \zeta)$ are Cartesian coordinates, $\mathbf{Q}$ is a vector of conservative variables, $\mathbf{E}$, $\mathbf{G}$ and $\mathbf{F}$ are flux vectors in the (ξ, η, ζ) coordinate system. The coordinates are normalized to a reference length L^*; dependent variables – to the corresponding freestream parameters, and pressure – to the doubled dynamic pressure $\rho^*_\infty U^{*2}_\infty$. Hereafter asterisks denote dimensional quantities. The dynamic viscosity is calculated using Sutherland's law $\mu = T^{3/2}(S+1)/(S+T)$, where $S = 110\,\mathrm{K}/T^*_\infty$. Details of the governing equations may be found in e.g. [7].

The Navier–Stokes equations are integrated using the in-house solver HSFlow (High Speed Flow), which implements an implicit finite-volume shock-capturing method with effectively the third-order approximation in space and second-order in time. Godunov-type TVD (total variation diminishing) scheme with Roe approximate Riemann solver is used. Reconstruction of the dependent variables at the grid cell edges is performed using van Leer slope limiter. The system of nonlinear algebraic equations, which approximates the governing partial differential equations, is solved using the Newton iteration method. At every iteration step, the corresponding linear algebraic system is solved using the GMRes (Generalized Minimal Residual) method. The HSFlow solver employs MPI technology and PETSc framework for distributed calculations on high-performance computing clusters. For parallel computations, the source structured grid is split into multiple zones with one-to-one interzone connectivity.

Note that this implicit shock-capturing numerical technique is universal and most efficient if the computational domain contains shock waves and other strong spatial inhomogeneities of the flow such as boundary-layer separations. Despite dissipative nature of the TVD scheme, the HSFlow solver allows simulations of boundary-layer stability including configurations with separation zones and/or strong non-linear effects [8, 9, 10]. Details on the numerical method may be found in [7].

2.2 Parameters of free stream and crossflow jet injection

Considered is a supersonic flow at free-stream Mach number $\mathrm{M}_\infty = 5.373$ over a sharp flat plate at zero angle of attack with an isolated crossflow jet injection. The flow parameters correspond to the laminar-turbulent transition experiments of Hyper-X model in the NASA LaRC 20-Inch Mach 6 Air Tunnel [11] and are gathered in Table 1. The earlier stability and numerical studies under these free-stream conditions were performed on a 5.5 degree compression corner [12, 13, 9, 14]. The reference length scale $L^* = 0.3161$ m corresponds to the distance from the plate leading edge to the corner point [11].

Table 1: Free-stream flow parameters

Parameter	Value	Parameter	Value
M_∞	5.373	T^*_∞	74.194 K
$\mathrm{Re}_{\infty,1}$	17.927×10^6 1/m	T^*_w	300 K
L^*	0.3161 m	γ	1.4
$\mathrm{Re}_{\infty,L}$	5.667×10^6	Pr	0.72

The problem is solved in two steps. First, a steady laminar flow field (base flow) is computed using the time-dependent method. Then, gas injection through a circular hole is turned on that forms a jet in supersonic crossflow (JISC). The injection hole diameter is $d^* = 1$ mm which is an arbitrary but realistic value. The injected gas is air – the same as in the free stream. The injection port is located in the $z = 0$ symmetry plane at $x_{inj} = 0.2$ where the unperturbed boundary-layer thickness is $\delta^*_{0.99} \approx 3.8$ mm. The similar jet was considered in [6] where hypersonic boundary-layer transition forced by wall injection was investigated numerically.

The main parameter that drives the jet is the total pressure $p_{0,inj}$ in an injection supply channel. Further consideration is focused on the case of sufficiently high injection pressure, when the injection is chocked forming a normal shock at the supply channel exit section, i.e. the injection Mach number is $\mathrm{M}_{inj} = 1$. In this case, from classical gas dynamics analysis, static injection pressure and temperature at the channel exit (critical section) are determined as

$$T^s_{inj} = T_{0,inj}\frac{2}{\gamma(\gamma+1)}, \quad p^s_{inj} = p_{0,inj}\left(\frac{2}{\gamma(\gamma+1)}\right)^{\frac{\gamma}{\gamma-1}},$$

where the superscript "s" denotes sonic conditions and subscript "0" denotes total value. The choked injection regime sets in if p^s_{inj} exceeds the wall static pressure p_w of the unperturbed boundary layer over the plate: $p^s_{inj} \geq p_w$. With that, an underexpanded supersonic jet is produced and its mass flow rate is independent of pressure variations in the supply channel.

For the jet to penetrate the boundary layer and form an equivalent roughness element, a sufficiently high injection pressure p^s_{inj} is required. Hereafter this parameter is $p^s_{inj} = 10.19p_w$, where $p_w = 1.037p_\infty$ is wall static pressure at injection port location for the unperturbed flat plate boundary layer. The injection temperature is chosen to be equal to the plate surface temperature, $T^s_{inj} = T_w$. The other parameters are deduced from these predefined values. The all injection parameters are given in Table 2.

Table 2: Wall injection parameters

Parameter	Value	Parameter	Value
d	1 mm $\mapsto$ 0.00316	T^s_{inj}	300 K $= T^*_w \mapsto$ 4.04
x_c	0.2	$T_{0,inj}$	360 K $\mapsto$ 4.852
p^s_{inj}	$10.19p_w \approx 10.57p_\infty = 0.2614$	M_{inj}	1.0
$p_{0,inj}$	$20p_\infty = 0.4948$	v^s_{inj}	0.374

The wall injection through a circular hole is modeled by the local boundary condition of Dirichlet type which is imposed over the hole area

$$\rho u|_{w,inj} = 0,\ \rho v|_{w,inj} = \rho_{inj} v^s_{inj},\ \rho w|_{w,inj} = 0,\ p_{w,inj} = p^s_{inj},\ T_{w,inj} = T^s_{inj}. \tag{1}$$

This allows to omit flow simulations inside a supply channel and thereby drastically simplify the grid topology. To check the validity of this simplification an additional calculations have been performed (see section 3.1).

2.3 Computation domain and boundary conditions

Computations are carried out for the flow over a flat plate. The computation domain in (x, y) plane is shown in Fig. 1. It is extruded along the spanwise z-axis to obtain the three-dimensional domain with $0 \leq z \leq 0.15$.

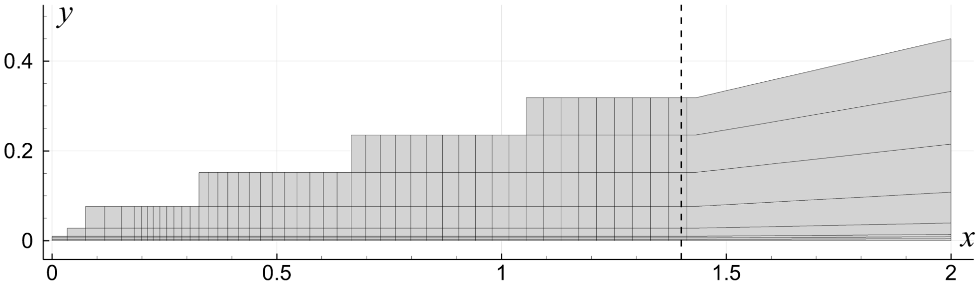

Figure 1: Computational domain in (x, y) plane. The solid lines show the edges of grid blocks. The dashed line shows the boundary of the buffer zone

The boundary conditions are: no-slip $u = v = w = 0$ and isothermal $T = T_w$ on the wall surface $y = y_{\min}$; the free-stream conditions $u = 1$, $v = w = 0$, $p = 1\big/\gamma \mathrm{M}^2_\infty$, $T = 1$ on the $x = x_{min} = 0$ (left) and $y = y_{max}$(top) boundaries; the linear extrapolation from the interior for the dependent variables u, v, w, p and T on the outflow boundaries $x = x_{max} = 2.0$ (right) and $z = z_{max}$ (front); the symmetry condition $\partial u/\partial n = \partial v/\partial n = \partial p/\partial n = \partial T/\partial n = 0$, $w = 0$ on the $z = 0$ plane. Special local boundary condition (1) is imposed on the hole outlet to imitate injection.

Computations are performed on an orthogonal grid with $2801 \times n_y \times 141$ nodes. The number of nodes in vertical direction n_y varies from 84 to 221 through the computational domain depending on the bow shock location. The grid contains 74.2×10^6 nodes in total. The grid step in the streamwise direction is $\Delta x \approx 5 \times 10^{-4}$ in the range of $0 < x \lesssim 1.4$, with clustering near the injection orifice to $\Delta x = 2 \times 10^{-4}$. In the wall normal direction the grid step is $\Delta y = 1.0 \times 10^{-4}$ within the boundary layer (about 120 grid lines) and increases towards the top boundary. The spanwise grid step is $\Delta z \approx 2 \times 10^{-4}$ in the range of $0 < z \lesssim 0.014$. Note, that the grid resolution is a way below of Kolmogorov length scale for homogeneous isotropic turbulence $l_K \sim \mathrm{Re}_{\infty,L}^{-3/4} = 0.086 \times 10^{-4}$. Therefore this numerical study falls within ILES (implicit large-eddy simulation) approach, which is assumed to be valid as large eddies domination is expected here.

Towards the outflow boundaries at $x \gtrsim 1.4$ and $z \gtrsim 0.014$ the grid cells are gradually enlarged up to very large values $\Delta x = 0.2$ and $\Delta z = 0.02$ to create a buffer (sponge) zone. In this part of computational domain the unsteady disturbances quickly dissipates because of large numerical viscosity. The solution in this zone is not physical and, therefore, it is not analyzed hereafter. To check the grid independence of the flow features, an additional grid was built twice more resolved in y direction ($\Delta y = 0.5 \times 10^{-4}$ within the boundary layer) but for a shorter domain $x < 0.6$. This mesh is used to clarify how the near-flow field is affected by the grid refinement. The time step during disturbances evolution simulation is $\Delta t = 0.0001$. Computations were carried out using multiprocessor high-performance computing cluster with distributed memory. Up to 302 CPU cores were employed simultaneously for a single case.

3. Flow in the injection region

3.1 Injection model validation

The proposed simple injection model (1) ignores the non-uniformity of injecting flow profile and the hole edge effects. To check if this simplification is applicable, an additional simulation was performed for the flow over the plate including the flow inside a supply channel. For this purpose a 3-D computational domain was built in the near-injection region ($0 < x < 0.3$, $-0.04 < z < 0.04$) including a short conical channel with the inflow section located at $y = -0.02$. On the inflow section of the channel, the boundary conditions of slowly vertically moving gas are imposed as $u = 0$, $v = 0.03$, $w = 0$, $p = 25.0 \approx p_{0,inj}$, $T = 4.846 \approx T_{0,inj}$ matching the total values of injected gas (see Table 2).

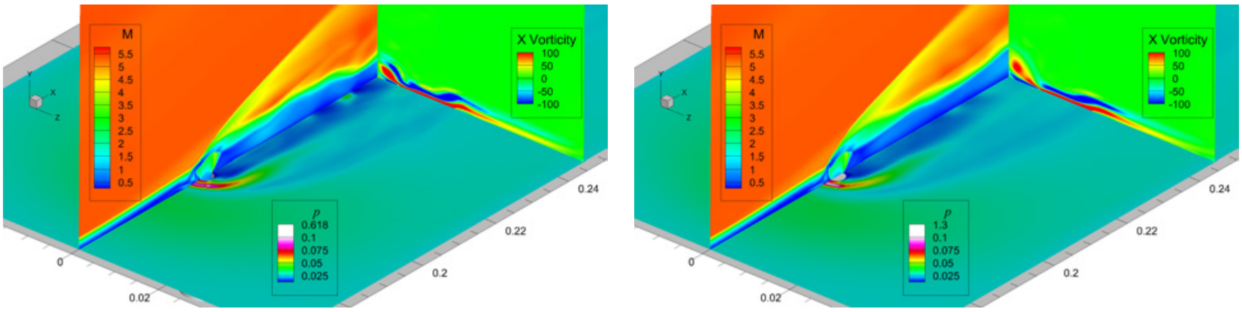

Figure 2: Flow structures in the injection region obtained in full simulation including a supply channel (left) and basic simulation with jet induced by the outlet boundary condition (1) (right). Shown are Mach numbers in the symmetry plane, wall pressure and x-vorticity in the $x = 0.24$ plane

The computed instantaneous near-injection flow fields resulted from the full simulation including the channel and the basic simulation using the outlet boundary condition (1) are shown in Fig. 2. It is clearly seen that all main flow structures discussed hereafter, are much the same in the both cases. This allows us to conclude that the employed simple injection model correctly simulates main features of the boundary-layer flow forced by an under-expanded jet in supersonic crossflow.

3.2 Grid dependence

The calculated flow field dependence on the grid resolution is evaluated using the base grid and the y-refined grid which is twice more resolved in the wall normal direction. The instantaneous vortex structure in the injection region computed on these grids is shown in Fig. 3. Hereafter the vortices are identified by Q-criterion, where Q is the second invariant of the velocity gradient tensor $Q = \frac{1}{2}\left(\|\mathbf{\Omega}\|^2 - \|\mathbf{S}\|^2\right)$, with $\mathbf{\Omega} = \frac{1}{2}\left(\nabla \boldsymbol{V} - (\nabla \boldsymbol{V})^T\right)$ and $\mathbf{S} = \frac{1}{2}\left(\nabla \boldsymbol{V} + (\nabla \boldsymbol{V})^{\mathrm{T}}\right)$. For convenience, the patterns shown hereafter are obtained by mirroring of the computed flow field versus the $z = 0$ symmetry plane.

Obviously, the fields are different for base and refined grids. As the grid is refined, more fine structures are exhibited in the instantaneous flow fields, which is inherent to the LES approach employed here. Nevertheless, the core large horseshoe-shaped vortex (HSV) has a similar location and sizes. Also, it is expected that time-averaged flow structures would be much the same by analogy with [6]. Hence, the base grid does suit the purpose of this study.

DOI: 10.13009/EUCASS2019-522

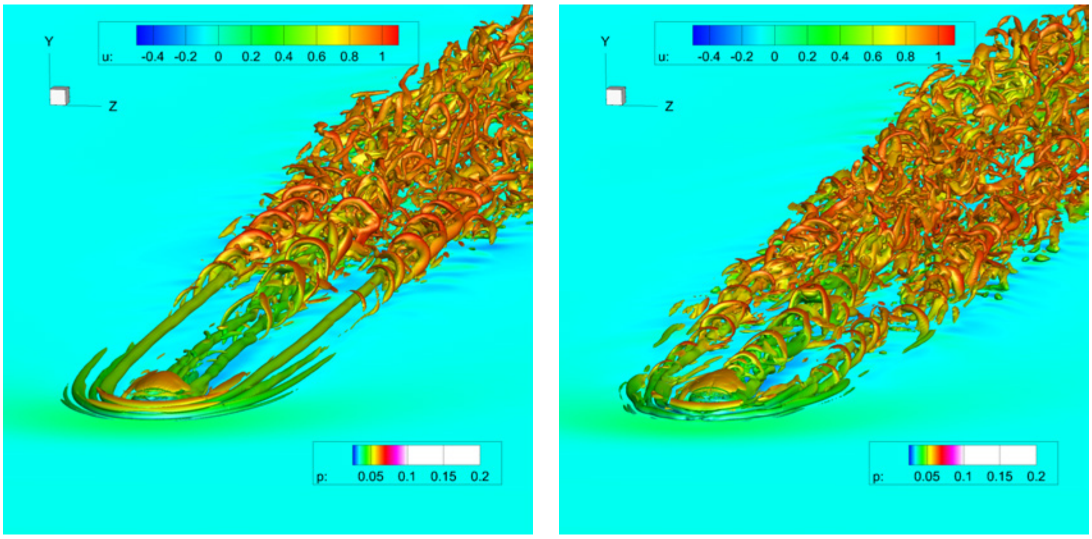

Figure 3: Instantaneous vortex structure in the injection region for base (left) and y-refined (right) grids. Shown are wall pressure and isosurface of $Q = 5000$ colored with u-velocity

3.3 Flow structure

The computed instantaneous flow field in the injection region is shown in Fig. 4 and 5. The well-known jet in supersonic crossflow (JISC) structures are clearly seen. There are the main bow shock due to the jet, the barrel shape of the under-expanded jet ending with a Mach disk, the separation zone ahead of the jet, the horseshoe vortices (HSV), and the primary counter-rotating longitudinal vortices (CRV).

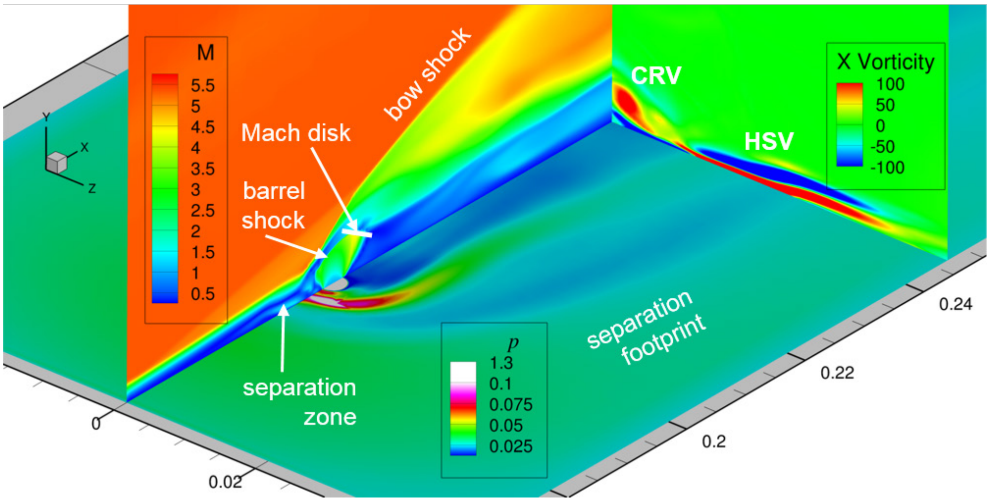

Figure 4: Flow structure in the injection region visualized with the Mach number field in the symmetry plane, wall pressure and x-vorticity at $x = 0.247$

Visual inspection of the near-jet flow structures, which are similar to that shown in Fig. 5, at different time instants reveals the following:

1. The separation zone ahead of the jet pulsates with rather low frequency.
2. The pulsating separation zone introduces perturbations of primary counter-rotating longitudinal vortices (2 in Fig. 5) moving downstream.
3. Over a short downstream distance, both HSV and CRV exhibit secondary instabilities in the form of small-sacle vortices wrapped around the primary vortices (3 in Fig. 5).
4. The small-scale vortices quickly evolves to hairpin structures, which are main drivers of turbulence in the boundary-layer flow

5. The disturbed boundary layer emits acoustic waves to the outer flow.

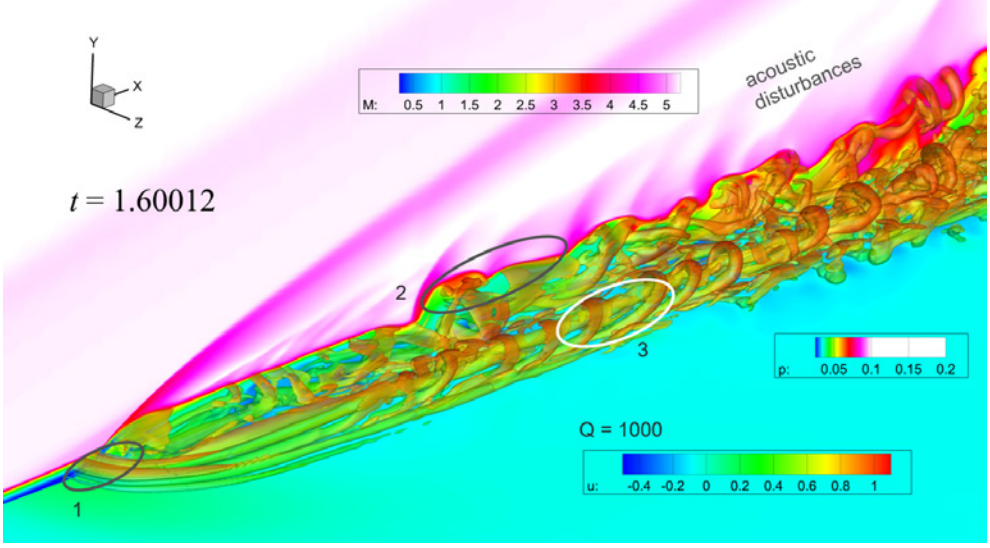

Figure 5: Flow structure in the injection region. Shown are semitransparent isosurface of Q-criterion colored by u-velocity, Mach number field in the symmetry plane and wall pressure. 1 – separation zone ahead of the jet, 2 – perturbation of CRV moving downstream, 3 – secondary instability of HCV

4. Instability evolution

The jet imposed onto the steady boundary layer leads to formation of unstable 3-D vortices evolving downstream. Instantaneous flow field in a large portion of the computational domain is shown in Fig. 6. The initial HSV and CRV structures quickly breakdown into small-scale chaotic-like structures resembling a young turbulent wedge. The hairpin vortices typical for laminar-turbulent process are also clearly seen. In this simulation the breakdown process is not initialized by any artificial unsteady forcing but occurs naturally due to numerical noise of very low intensity. This allows us to assume that the system of boundary-layer and injection jet is absolutely unstable, such that any numerical perturbations are amplified in the injection region to appreciable amplitudes and feed the breakdown process. Note, that the vortical structure in Fig. 6 is very similar to that induced by an isolated cylindrical roughness (e.g. see the DNS solution of Chaudhry et al. in Fig. 15 of Ref. [4]).

The pressure disturbances on the plate surface, $p'_w(x, z)$, is shown in Fig. 7. Here the disturbance field is obtained by subtracting the base unperturbed flow field (without injection) from the field at a certain time instant, $p'(t) = p(t) - p(t = 0)$. The wall pressure pattern allows us to evaluate the lateral spread angle of the disturbance field as $\phi \approx 3°$. This value agrees well with the lateral spread angles of turbulent spots obtained experimentally [15] and numerically [16].

4.1 Spectra

Wave content of the disturbance field can be analyzed using spatial-temporal spectra. Figure 8 shows 2-D spectra (absolute values of 2-D Fourier transform vs. z and t) of the wall pressure disturbances in various x-stations. Here β is z-component of the wave vector and ω is angular frequency of a wave $\sim q(x, y)\exp(i\beta z - i\omega t)$. In the local-parallel approximation, the amplitude function can be expressed as $q(x, y) \approx \hat{q}(y)\exp(i\alpha x)$, where $\alpha = \alpha(\beta, \omega)$ can be treated as an eigenvalue and $\theta = \tan^{-1}(\beta/\alpha)$ is a wave-front angle.

In the whole, the spectra are rather broad starting from the station $x = 0.3$ lying near the jet ($x_{inj} = 0.2$). As x increases the spectrum broadens further and starts to resemble an isotropic turbulence. Among the all spectral components, it should be highlighted the mean flow distortions of zero frequency $\omega = 0$ and waves of low frequency $\omega \approx 45$. These components are clearly seen in the all x-stations. The $(0, 0)$ component represents the mean boundary-layer flow structures, which are associated with the near-field distortion because of the injected gas and the far-field distortion due to laminar-turbulent transition. The waves of $\omega = 0, \beta > 0$ correspond to longitudinal vortices (near-wall streaks). The waves of $\omega \approx 45$ are presumably related to the low-frequency pulsation of the separation zone ahead the jet. Starting from the station $x \approx 1.0$ the spectra contain the high-frequency peaks of $\omega \approx 350$ associated with

DOI: 10.13009/EUCASS2019-522

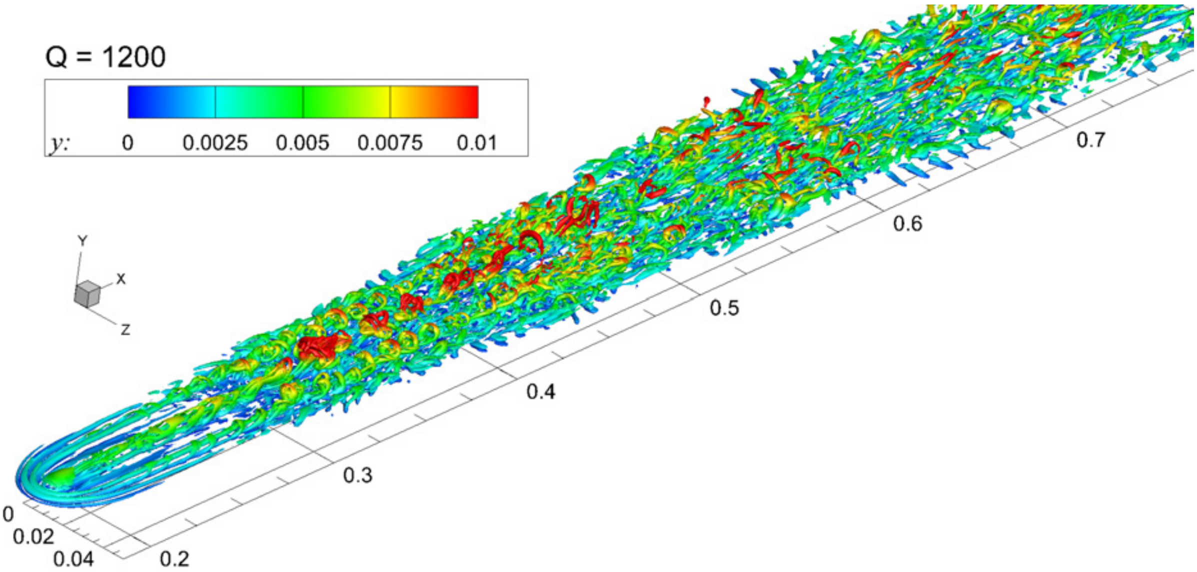

Figure 6: Instantaneous vortex structure downstream the injection visualized with isosurface of Q-criterion colored by the distance from the wall

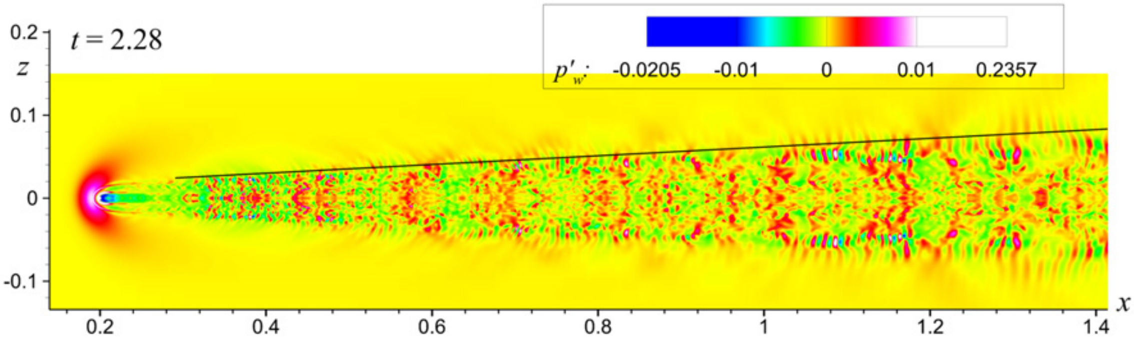

Figure 7: Instantaneous wall pressure disturbance field. Inclined line indicates the core-part of the turbulent wedge

the secondary instability of HSV and CRV. These small-scale structures are modulated with wave-numbers $\beta \approx 45$ corresponding to low-frequency oscillations of the primary vortices.

4.2 Skin friction

The beginning of laminar-turbulent transition and the streamwise length of transitional region can be evaluated using distributions of the skin friction coefficient

$$C_{fx} = \tau_w^* \Big/ \tfrac{1}{2}\rho^* V_\infty^* = \left[\mu \frac{\partial u}{\partial n}\right]_w \Big/ \tfrac{1}{2} Re_\infty \ .$$

Figure 9 shows instantaneous and time-averaged patterns of $C_{fx}(x, z)$ on the plate surface. These patterns are typical for turbulent wedge including streaky structures. The visual assessment of the lateral spread angle based on the skin friction distribution gives $\phi \approx 2.3°$ that is less than that estimated using the wall pressure pattern (see Fig.7). Nevertheless, this value falls within the scatter range of available data on the turbulence spreading [15, 16].

Figure 4.2 shows the distributions of skin friction coefficient $C_{fx}(x)$ along the center line $z = 0$. The black lines show the skin friction for laminar and turbulent flows. The laminar distribution of C_{fx} corresponds to the unperturbed

DOI: 10.13009/EUCASS2019-522

steady flow without injection. The turbulent distribution of C_{fx} is obtained from the Van Driest II correlation [17]

$$\frac{0.242}{b\sqrt{C_{fx}T_w}}\left[\arcsin\left(\frac{2b^2-a}{\sqrt{a^2+4b^2}}\right)+\arcsin\left(\frac{a}{\sqrt{a^2+4b^2}}\right)\right]=0.41+\lg\left(Re_xC_{fx}\right)-\omega_\mu\lg\left(T_w\right),$$

$$a=\frac{1}{T_w}\left(1+r_t\frac{\gamma-1}{2}M_\infty^2\right)-1, b=\frac{r_t}{T_w}\frac{\gamma-1}{2}M_\infty^2, r_t=\sqrt[3]{\mathrm{Pr}}\simeq 0.9, \omega_\mu=0.76, Re_x=xRe_\infty,$$

where r_t is the recovery factor for turbulent boundary layer and ω_μ is the exponent in a power law relation between temperature and viscosity.

The skin friction approaches the turbulent level over a rather short distance from the jet. Significant overshoots of the turbulent correlation level indicates the presence of highly nonlinear transitional regime which is not relaxed to the equilibrium turbulent state yet. Large oscillations of the time-averaged distribution (blue line) are due to a relatively short time period in the averaging procedure. Altogether, the crossflow jet injection is a very effective method of tripping the boundary-layer flow at high speeds.

5. Conclusions

Implicit large-eddy simulations (ILES) have been performed to investigate 3-D disturbances propagating over a flat plate at the free-stream Mach number $M_\infty = 5.373$ with wall injection through a circular hole. The injection produces a barrel-shaped under-expanded jet in supersonic crossflow (JISC) and a system of unstable vortices evolving downstream. The nonlinear breakdown of these vortices leads to laminar-turbulent transition which ends with the turbulent wedge.

The ILES computations are carried out using the in-house Navier–Stokes solver HSFlow implementing an implicit finite-volume shock-capturing method with the second-order approximation in space and time. It is shown that this code is able to simulate highly nonlinear dynamics of disturbances induced by JISC up to the stage of “young” turbulent wedge.

The computed JISC flow is very similar to that past an isolated roughness element. In the both cases, the observed flow structures include: bow shock, upstream separation zone, horseshoe vortices (HSV), primary counter-rotating longitudinal vortices (CRV), small-scale structures associated with secondary instability of the primary HSV and CRV.

The injection jet leads to very quick laminar-turbulent transition without any artificial unsteady forcing. Instability evolves naturally due to numerical noise of very low intensity. This allows us to assume that the system of boundary-layer and injection jet is absolutely unstable, such that any numerical perturbations are amplified in the injection region to appreciable amplitudes and feed the breakdown process.

The wall pressure disturbance spectra exhibit low-frequency harmonics associated with pulsations in the separation zone ahead JISC, as well as high-frequency harmonics associated with secondary instability of HSV and CRV. The latter quickly evolve to hairpin vortices, which drive a self-sustaining process of turbulence production in the boundary-layer flow. Ultimately a turbulent wedge is formed at a relatively short distance from the jet. The lateral spreading angle of this wedge equals to 2.3°… 3.0°. These values fall within the scatter range of experimental and DNS data on spreading of turbulent spots in high-speed boundary layer flows.

The numerically predicted skin friction coefficient exhibits a rapid increase with significant overshoot of the turbulent level. Similar to the flow past an effective roughness element, the transition region is short and it is located at a small distance downstream the jet. Thus, this numerical study confirms that JISC is very effective in tripping of high-speed boundary layer flows. As contrasted to roughness elements, the injection jets are adjustable to a broad range of flow conditions. Moreover, the injection of relatively cold gas reduces thermal loads that is of critical importance for high-speed applications.

6. Acknowledgments

This work has been carried out using computing resources of the federal collective usage center Complex for Simulation and Data Processing for Mega-science Facilities at NRC “Kurchatov Institute”, http://ckp.nrcki.ru/ with financial support of the Russian Foundation for Basic Research (project No. 18-08-01295).

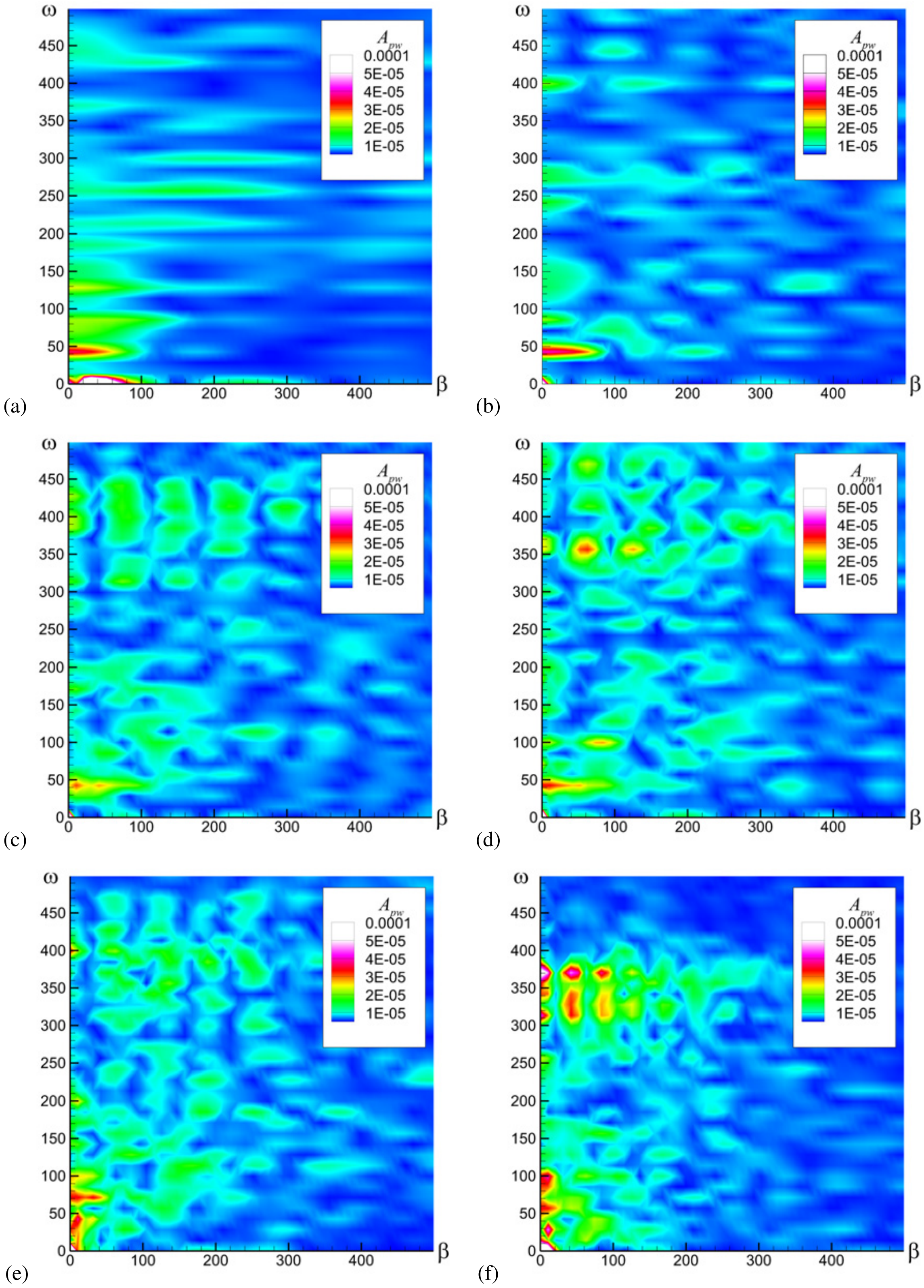

Figure 8: Wall pressure disturbance spectra at different x-stations; (a) – (f) correspond to x = 0.3, 0.5, 0.8, 1.0, 1.2, 1.35, respectively

DOI: 10.13009/EUCASS2019-522

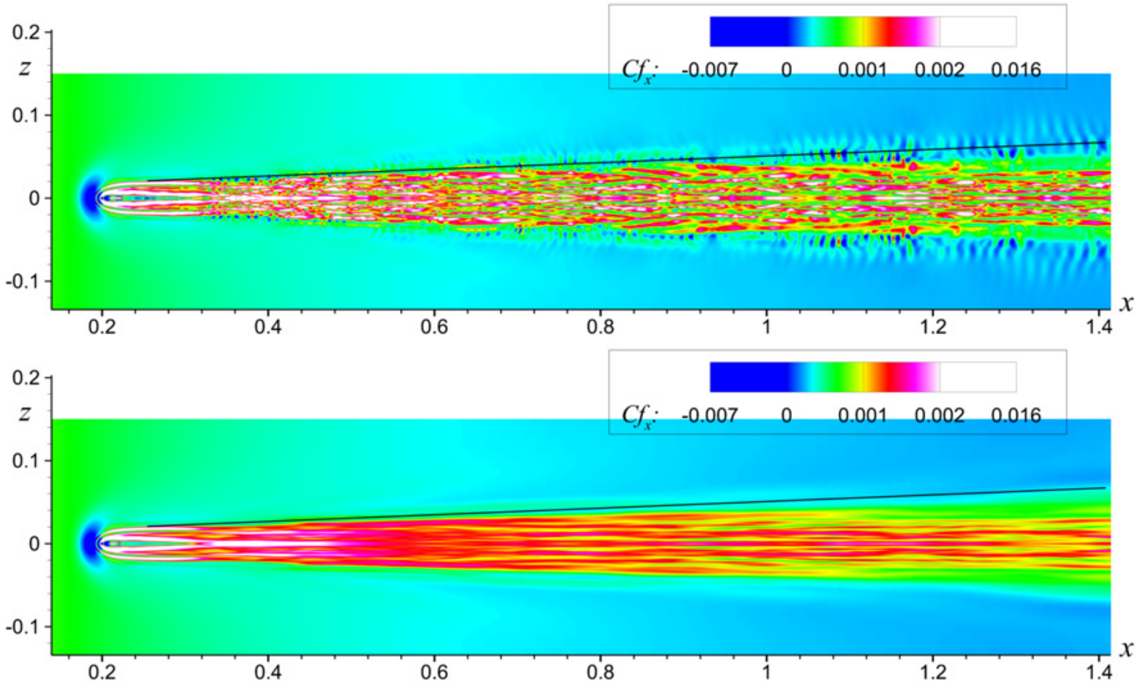

Figure 9: Skin friction coefficient $C_{fx}(x, z)$ instantaneous (top) and time-averaged (bottom). The black inclined lines indicate the core-part of the turbulent wedge

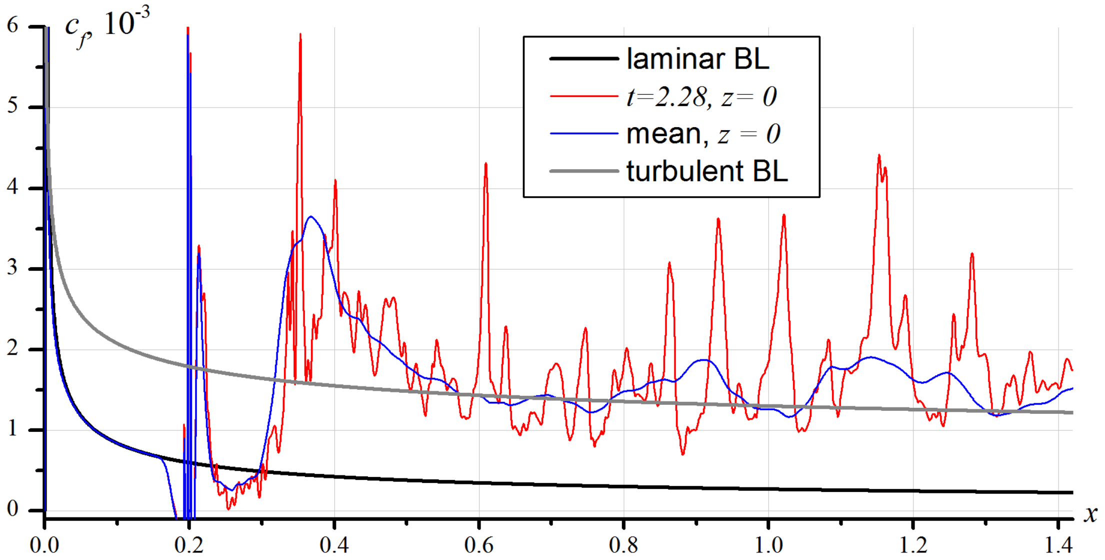

Instantaneous (red line) and time-averaged (blue line) distributions of the skin friction coefficient along the center line $z = 0$; "laminar BL" – steady unperturbed boundary-layer flow without injection; "turbulent BL" – Van Driest II correlation for turbulent boundary layer

DOI: 10.13009/EUCASS2019-522

References

[1] Scott Berry and Thomas Horvath. Discrete roughness transition for hypersonic flight vehicles. AIAA paper 2007-307, jan 2007.

[2] Scott Berry, Robert Nowak, and Thomas Horvath. Boundary layer control for hypersonic airbreathing vehicles. AIAA paper 2004-2246, jun 2004.

[3] Brett Bathel, Paul Danehy, Jennifer Inman, David Alderfer, and Scott Berry. PLIF visualization of active control of hypersonic boundary layers using blowing. AIAA paper 2008-4266, jun 2008.

[4] Ross S. Chaudhry, Pramod K. Subbareddy, Ioannis Nompelis, and Graham V. Candler. Direct numerical simulation of roughness-induced transition in the VKI mach 6 tunnel. AIAA paper 2015-0274, American Institute of Aeronautics and Astronautics, 2015.

[5] Prakash Shrestha and Graham V. Candler. Direct numerical simulation of high-speed transition due to roughness elements. *Journal of Fluid Mechanics*, 868:762–788, apr 2019.

[6] E. Orlik, I. Fedioun, and N. Lardjane. Hypersonic boundary-layer transition forced by wall injection: A numerical study. *Journal of Spacecraft and Rockets*, 51(4):1306–1318, jul 2014.

[7] I. V. Egorov, A. V. Novikov, and A. V. Fedorov. Direct numerical simulation of the laminar–turbulent transition at hypersonic flow speeds on a supercomputer. *Computational Mathematics and Mathematical Physics*, 57(8):1335–1359, 2017.

[8] Dmitry Bountin, Timur Chimitov, Anatoly Maslov, Andrey Novikov, Ivan Egorov, Alexander Fedorov, and Sergey Utyuzhnikov. Stabilization of a hypersonic boundary layer using a wavy surface. *AIAA Journal*, 51(5):1203–1210, 2013.

[9] Andrey Novikov, Ivan Egorov, and Alexander Fedorov. Direct numerical simulation of wave packets in hypersonic compression-corner flow. *AIAA Journal*, 54(7):2034–2050, jul 2016.

[10] Pavel V. Chuvakhov and Alexander V. Fedorov. Spontaneous radiation of sound by instability of a highly cooled hypersonic boundary layer. *Journal of Fluid Mechanics*, 805:188–206, September 2016.

[11] Scott A. Berry, Michael DiFulvio, and Matthew K. Kowalkowski. Forced boundary-layer transition on X-43 (hyper-X) in NASA LaRC 20-inch mach 6 air tunnel. NASA/TM 2000-210316, NASA Langley Research Center, 2000.

[12] Hongwu Zhao and Ponnapalam Balakumar. Nonlinear disturbance evolution across a hypersonic compression corner. *AIAA Journal*, 43(5):1034–1041, 2005.

[13] I. V. Egorov, A. V. Novikov, and A. V. Fedorov. Numerical modeling of the disturbances of the separated flow in a rounded compression corner. *Fluid Dynamics*, 41(4):521–530, jul 2006.

[14] Andrey V. Novikov. Transition induced by a wave train in a supersonic boundary layer over a compression ramp. AIAA paper 2017-4517, American Institute of Aeronautics and Astronautics, June 2017.

[15] Michael C. Fischer. Spreading of a turbulent disturbance. *AIAA Journal*, 10(7):957–959, jul 1972.

[16] Jeroen Van den Eynde and Johan Steelant. Compressibility and temperature effects on turbulent spot growth. In *HiSST: International Conference on High-Speed Vehicle Science Technology, 26–29 November 2018, Moscow*, 2018.

[17] E. R. Van Driest. The problem of aerodynamic heating. *Aeronautical Engineering Review*, 15(8):26–41, 1956.